

A fast majorize-minimize algorithm for the recovery of sparse and low rank matrices

Yue Hu, *Student Member, IEEE*, Sajan Goud, *Student Member, IEEE*, Mathews Jacob, *Member, IEEE*

Abstract

We introduce a novel algorithm to recover sparse and low-rank matrices from noisy and undersampled measurements. We pose the reconstruction as an optimization problem, where we minimize a linear combination of data consistency error, non-convex spectral penalty, and non-convex sparsity penalty. We majorize the non-differentiable spectral and sparsity penalties by quadratic expressions to realize an iterative, three-step, alternating minimization scheme. Since each of these steps can either be evaluated analytically or using fast schemes, we obtain a computationally efficient algorithm. We demonstrate the utility of the algorithm in the context of dynamic MRI reconstruction from sub-Nyquist sampled measurements. The results show a significant improvement in signal to noise ratio and image quality compared to classical dynamic imaging algorithms. We expect the proposed scheme to be useful in a range of applications including video restoration and multidimensional MRI.

I. INTRODUCTION

The recovery of a low-rank or approximately low-rank matrix from very few measurements of its entries has received a lot of attention in recent years, mainly due to its application in machine learning, computer vision and recommendation systems [1], [2]. Our own motivation in this area is to use this framework to recover dynamic imaging/video data from sparse and noisy measurements. Several researchers have posed the reconstruction of dynamic image data as the recovery of a low-rank Casoratti matrix, whose columns correspond to spatial pixels and the rows correspond to temporal intensity variations of the pixels [3], [4], [5], [6], [7]. In addition, the low-rank matrix may be known to be additionally sparse in a specified domain. For example, each of the frames of a dynamic imaging dataset can have sparse wavelet coefficients or gradients [8]. It is known that sparsity and low-rank properties are somewhat complementary [1]; most randomly selected low-rank matrices are not sparse and most sparse random matrices are not low-rank [9]. However, there are matrices that are simultaneously sparse and low-rank. For example, a matrix with only one non-zero entry will have a sparsity of one and will be of unit rank. We exploit the fewer degrees of the freedom of the set of matrices that are simultaneously sparse and low-rank, compared to only sparse or only low-rank matrices, to significantly reduce the number of measurements.

Y. Hu is with the Department of Electrical and Computer Engineering, University of Rochester, NY, USA. S. Goud and M. Jacob is with the Department of Biomedical Engineering, University of Rochester, NY, USA. e-mail: (see <http://www.cbig.rochester.edu>). This work is supported by NSF award CCF-0844812.

We, as well as other researchers, have demonstrated the utility of modeling dynamic imaging dataset as a sparse and low-rank Casoratti matrix [5], [6], [10], [11].

In this work, we focus on non-convex spectral and sparsity penalties to further decrease the number of measurements required for recovery. Specifically, we consider Schatten- p functionals, which are the extensions of the classical nuclear norm spectral penalty. This choice is inspired by the recent success of non-convex compressed sensing schemes that rely on $\ell_p; p < 1$ penalties [12], [13]. Similar to the ℓ_p vector penalty, the Schatten- p functions cease to be norms and are non-convex for $p < 1$. We also use non-convex sparsity penalties as in [14], [12], [13]. Thus, we pose the recovery of the sparse and low-rank matrix as a non-convex optimization problem, where the cost function is a linear combination of the data consistency term, non-convex spectral penalty and non-convex sparsity penalty. Most of the current matrix recovery algorithms are variants of iterative singular value thresholding [15], [16], [17]. Unfortunately, it is not easy to adapt this scheme to our case since our penalty is a linear combination of non-convex spectral and sparsity functions; it is difficult to efficiently evaluate the proximal mapping of the linear combination of non-convex penalties. Huang et al., has recently introduced a scheme based on multiple proximal mappings to minimize a criterion with two convex priors [18]. This algorithm can be extended to the matrix recovery problem, when the priors are convex. However, the proximal mappings will not have closed form expressions when non-convex penalties are used; this makes it difficult to directly extend the algorithm in [18] to our case.

We introduce a novel majorize-minimize (MM) algorithm to recover sparse and low-rank matrices from undersampled measurements. In contrast to current matrix recovery schemes that majorize the data consistency term, we majorize each of the penalty terms with quadratic functions. We use the property of unitarily invariant matrix penalties to majorize the spectral penalty. This majorization of the penalty terms enables us to solve for the matrix using a three step alternating minimization scheme with closed form shrinkage rules. The iterative algorithm alternates between the three simple steps: **(i)** the solution of a linear system of equations **(ii)** a singular value shrinkage, and **(iii)** gradient shrinkage. The linear system of equations can be solved either using analytical expressions or a few conjugate gradient steps. Both the shrinkage steps are obtained as the proximal mappings [19] of new matrix functions, which are related to the original spectral and sparsity penalties. Thanks to the property of convex conjugate matrix functions, these shrinkage rules have analytical expressions, even when non-convex penalties are used. Since each step of the algorithm can be evaluated analytically or using fast schemes, the algorithm is computationally very efficient. When convex penalties (nuclear norm and total variation norm) are used, the proposed MM scheme is equivalent to the VS scheme, which was introduced in our earlier work [6]. However, the proximal mappings in the VS scheme do not have closed form expressions when non-convex penalties are used. While the proximal mappings for the non-convex penalties can be approximated as shown in [20], we observe that the resulting approximate VS algorithm is significantly slower than the corresponding MM scheme. We also introduce a continuation scheme to accelerate the convergence of the algorithm. In addition to providing fast algorithms, this approach makes the algorithm robust to local minima effects. Specifically, we use a sequence of criteria with gradually increasing complexity, while using the solution from the previous iteration to initialize the new criterion. Similar homotopy continuation schemes are used in non-convex compressed sensing to minimize

local minima effects [21].

The rest of the paper is organized as follows. We briefly review the background literature in Section II to make the paper self contained. We introduce the majorize-minimize algorithm in Section III, while its numerical implementation is described in Section IV. We study the convergence of the algorithm and its utility in practical applications in the results Section V.

II. BACKGROUND

A. Matrix recovery using nuclear norm minimization

Current theoretical results indicate that a matrix $\mathbf{\Gamma} \in \mathbb{R}^{m \times n}$ of rank r ; $r \leq \min(m, n)$ can be perfectly recovered from its linear measurements $\mathbf{b} = \mathcal{A}(\mathbf{\Gamma})$ [2], [1]. This recovery can be formulated as the constrained optimization problem:

$$\mathbf{\Gamma}^* = \arg \min_{\mathbf{\Gamma}} \|\mathcal{A}(\mathbf{\Gamma}) - \mathbf{b}\|^2 \text{ such that } \text{rank}(\mathbf{\Gamma}) \leq r. \quad (1)$$

To realize computationally efficient algorithms, the above problem is often reformulated as an unconstrained convex optimization scheme

$$\mathbf{\Gamma}^* = \arg \min_{\mathbf{\Gamma}} \underbrace{\|\mathcal{A}(\mathbf{\Gamma}) - \mathbf{b}\|^2 + \lambda \|\mathbf{\Gamma}\|_*}_{\mathcal{C}(\mathbf{\Gamma})}, \quad (2)$$

where $\|\mathbf{\Gamma}\|_*$ is the nuclear norm of the matrix $\mathbf{\Gamma} = \sum_{i=1}^{\min(m,n)} \sigma_i \mathbf{u}_i \mathbf{v}_i^H$. This penalty is the convex relaxation of the rank and is defined as the sum of the singular values of $\mathbf{\Gamma}$: $\|\mathbf{\Gamma}\|_* = \sum_{i=1}^{\min(m,n)} \sigma_i$.

B. Majorize-minimize algorithms

Majorize-minimize algorithms rely on a surrogate function $\mathcal{S}(\mathbf{\Gamma}, \mathbf{\Gamma}_n)$ that majorizes the objective function $\mathcal{C}(\mathbf{\Gamma})$ using the current iterate $\mathbf{\Gamma}_n$. The surrogate function equals to the objective function at the tangent $\mathbf{\Gamma}_n$ (i.e., $\mathcal{S}(\mathbf{\Gamma}_n, \mathbf{\Gamma}_n) = \mathcal{C}(\mathbf{\Gamma}_n)$) and is larger than the objective function elsewhere:

$$\mathcal{S}(\mathbf{\Gamma}, \mathbf{\Gamma}_n) \geq \mathcal{C}(\mathbf{\Gamma}); \forall \mathbf{\Gamma}. \quad (3)$$

The successive minimization of the majorant function $\mathcal{S}(\mathbf{\Gamma}, \mathbf{\Gamma}_n)$ ensures that the cost function $\mathcal{C}(\mathbf{\Gamma})$ decreases monotonically. This property guarantees global convergence for convex cost functions. We rely on homotopy continuation schemes to minimize local minima problems, when non-convex cost functions are used.

C. Matrix recovery using iterative singular value thresholding

The common approaches to solve for (2) involve different flavors of iterative singular value thresholding (IST) [15], [16], [17]. These schemes majorize the data-consistency term in (2) with a quadratic expression:

$$\|\mathcal{A}(\mathbf{\Gamma}) - \mathbf{b}\|^2 \leq \tau \|\mathbf{\Gamma} - \mathbf{Z}_n\|^2 + c_n. \quad (4)$$

Here, τ is a constant such that $\tau \mathcal{I} \geq \mathcal{A}^t \mathcal{A}$, c_n is a constant that is independent of $\mathbf{\Gamma}$, and $\mathbf{Z}_n = \mathbf{\Gamma}_n - \mathcal{A}^t(\mathcal{A}(\mathbf{\Gamma}_n) - \mathbf{b})/\tau$. Here, \mathcal{I} is the identity operator. Thus, we have

$$\mathcal{C}(\mathbf{\Gamma}) \leq \underbrace{\tau \|\mathbf{\Gamma} - \mathbf{Z}_n\|^2 + \lambda \|\mathbf{\Gamma}\|_*}_{\mathcal{C}_{\text{maj}}(\mathbf{\Gamma})} + c_n \quad (5)$$

The minimization of the above expression is termed as the proximal mapping of \mathbf{Z}_n , associated with the nuclear norm penalty [19]. This proximal mapping has an analytical solution [15]:

$$\mathbf{\Gamma}_{n+1} = \sum_{i=1}^{\min(m,n)} (\sigma_i - \lambda/2\tau)_+ \mathbf{u}_i \mathbf{v}_i^H, \quad (6)$$

where, $\mathbf{u}_i, \mathbf{v}_i$ are the singular vectors and σ_i are the singular values of \mathbf{Z}_n . The thresholding function in (6) is defined as

$$(\sigma)_+ = \begin{cases} \sigma & \text{if } \sigma \geq 0 \\ 0 & \text{else.} \end{cases} \quad (7)$$

Unfortunately, it is not straightforward to adapt this algorithm to optimization schemes with multiple non-differentiable penalty terms (e.g. spectral and sparsity penalties).

D. Unitarily invariant matrix functions

We focus on the general class of unitarily invariant spectral penalties, which satisfy the following property:

$$\phi(\mathbf{\Gamma}) = \phi(\mathbf{V}\mathbf{\Gamma}\mathbf{U}), \forall \mathbf{\Gamma} \in \mathbb{R}^{m \times n}, \forall \mathbf{U} \in \mathcal{U}_n, \forall \mathbf{V} \in \mathcal{U}_m. \quad (8)$$

Here, \mathcal{U}_m is the set of $m \times m$ unitary matrices. The above definition implies that $\phi(\mathbf{\Gamma})$ is invariant to pre and post-multiplication of $\mathbf{\Gamma}$ by unitary matrices. This class has several attractive properties, which are valuable in realizing fast algorithms. Specifically, Lewis et al. have shown that unitarily invariant convex matrix functions are fully characterized by composite functions of the singular values of the matrix [22]. If $\boldsymbol{\sigma}(\mathbf{\Gamma})$ denotes the $\min(m, n)$ dimensional vector of singular values of $\mathbf{\Gamma}$, any unitarily invariant penalty can be specified as

$$\phi(\mathbf{\Gamma}) = \rho(\boldsymbol{\sigma}(\mathbf{\Gamma})). \quad (9)$$

Here $\rho : \mathbb{R}^{\min(m,n)} \rightarrow \mathbb{R}$ is a function that is invariant under sign changes and permutations of the elements of $\boldsymbol{\sigma}(\mathbf{\Gamma})$. An interesting case is when $\rho(\boldsymbol{\sigma}) = \sum_{i=1}^{\min(m,n)} \mu(\sigma_i)$, where $\mu : \mathbb{R} \rightarrow \mathbb{R}$ is a function that is invariant to sign of σ_i . This class includes most of the spectral penalties of practical interest. For example, the Schatten p spectral norms correspond to $\mu(\sigma) = |\sigma|^p$. These penalties are convex and are norms when $p \geq 1$. Clearly, the nuclear norm is a special case of Schatten p -norms, when $p = 1$. Thanks to the results by Lewis et al., [22], many of the properties of vector functions can be extended to matrices. For example, the subgradient of $\phi(\mathbf{\Gamma})$ is given by [22] $\partial\phi(\mathbf{\Gamma}) = \{\mathbf{U} \text{diag}(\boldsymbol{\delta}) \mathbf{V}^* \mid \boldsymbol{\delta} \in \partial\rho(\boldsymbol{\sigma}(\mathbf{\Gamma}))\}$. Here $\mathbf{\Gamma} = \mathbf{U} \text{diag}(\boldsymbol{\sigma}(\mathbf{\Gamma})) \mathbf{V}^*$ is the singular value decomposition of $\mathbf{\Gamma}$. When $\rho(\boldsymbol{\sigma}) = \sum_i \mu(\sigma_i)$, we have

$$\partial\phi(\mathbf{\Gamma}) = \sum_{i=1}^{\min(m,n)} \partial\mu(\sigma_i) \mathbf{u}_i \mathbf{v}_i^H, \quad (10)$$

where $\partial\mu(\sigma_i)$ is the subgradient of $\mu(\sigma_i)$. Similarly, the convex conjugate of unitarily invariant penalties can be easily derived in terms of the convex conjugates of the corresponding μ functions. We use these results to extend the MM algorithms, which are originally developed for vector recovery, to matrix recovery problems.

E. Dynamic imaging using matrix recovery schemes

Our motivation in developing this algorithm is to use it in dynamic imaging and video restoration. We denote the spatio-temporal signal as $\gamma(\mathbf{x}, t)$, where \mathbf{x} is the spatial location and t denotes time. We denote the sparse and noisy measurements to be related to γ as $\mathbf{b} = \mathcal{A}(\gamma) + \mathbf{n}$, where \mathcal{A} is the measurement operator and \mathbf{n} is the noise process. The vectors corresponding to the temporal profiles of the voxels are often highly correlated or linearly dependent. The spatio-temporal signal $\gamma(\mathbf{x}, t)$ can be re-arranged as a Casoratti matrix to exploit the correlations [3], [4], [6], [7]:

$$\mathbf{\Gamma} = \begin{bmatrix} \gamma(\mathbf{x}_0, t_0) & \dots & \gamma(\mathbf{x}_0, t_{n-1}) \\ \vdots & & \\ \gamma(\mathbf{x}_{m-1}, t_0) & \dots & \gamma(\mathbf{x}_{m-1}, t_{n-1}) \end{bmatrix} \quad (11)$$

The i^{th} row of $\mathbf{\Gamma}$ corresponds to the temporal intensity variations of the voxel \mathbf{x}_i . Similarly, the j^{th} column of $\mathbf{\Gamma}$ represents the image at the time point t_j . Since the rows of this $m \times n$ matrix are linearly dependent, the rank of $\mathbf{\Gamma}$ is given by $r < \min(m, n)$. We will refer to the dynamic imaging dataset either as $\gamma(\mathbf{x}, t)$ or as $\mathbf{\Gamma}$ in the remaining sections. The low-rank structure of dynamic imaging datasets was used to recover them from undersampled Fourier measurements by several authors [3], [4], [6], [7], [23].

III. MAJORIZE MINIMIZE ALGORITHM FOR MATRIX RECOVERY

We introduce the problem formulation and the algorithm in this section. The details of the numerical implementation are covered in Section IV.

A. Matrix recovery using sparsity and spectral penalties

To exploit the low-rank and sparsity of the matrix in the transform domain (specified by \mathbf{R} and \mathbf{C}), we formulate the matrix recovery as the constrained optimization scheme:

$$\begin{aligned} \mathbf{\Gamma}^* &= \arg \min_{\mathbf{\Gamma}} \|\mathcal{A}(\mathbf{\Gamma}) - \mathbf{b}\|^2 \\ &\text{such that } \{\text{rank}(\mathbf{\Gamma}) \leq r, \|\mathbf{R}^H \mathbf{\Gamma} \mathbf{C}\|_{\ell_0} < K\} \end{aligned} \quad (12)$$

We rewrite the above constrained optimization problem using Lagrange's multipliers and relax the penalties to obtain

$$\mathbf{\Gamma}^* = \arg \min_{\mathbf{\Gamma}} \|\mathcal{A}(\mathbf{\Gamma}) - \mathbf{b}\|^2 + \lambda_1 \phi(\mathbf{\Gamma}) + \lambda_2 \psi(\mathbf{\Gamma}). \quad (13)$$

Here, the spectral penalty ϕ is the relaxation of the rank constraint. We choose it as the class of Schatten p matrix penalties ($\mu(\sigma) = |\sigma|^p$), specified by

$$\phi(\mathbf{\Gamma}) = \sum_{i=1}^{\min(m,n)} \sigma_i(\mathbf{\Gamma})^p. \quad (14)$$

Similarly, we specify the sparsity penalty as $\psi(\mathbf{\Gamma}) = \|\mathbf{R}^H \mathbf{\Gamma} \mathbf{C}\|_{\ell_{p_2}}^{p_2}$, which is the ℓ_{p_2} norm of the matrix entries, specified by:

$$\|\mathbf{\Gamma}\|_{\ell_p}^p = \sum_{i,j} |\Gamma_{i,j}|^p. \quad (15)$$

When $p_1, p_2 \geq 1$, the cost function (13) is convex and hence has a unique minimum. We now generalize the sparsity penalty to account for non-separable convex and non-convex total variation-like penalties:

$$\psi(\gamma) = \int_{\mathbb{R}^3} \|\nabla \gamma(\mathbf{x}, t)\|_2^{p_2} d\mathbf{x} dt, \quad (16)$$

which are widely used in imaging applications [24], [25]. The above penalty is often implemented using finite difference operators. Rewriting the above expression in terms of the matrix $\mathbf{\Gamma}$, we get

$$\psi(\mathbf{\Gamma}) = \varphi(\mathbf{P}) = \|\mathbf{P}\|_{\ell_{p_2}}^{p_2}, \quad (17)$$

where, $\mathbf{P} = \sqrt{\sum_{i=1}^q |\mathbf{R}_i^H \mathbf{\Gamma} \mathbf{C}_i|^2}$. Here $\mathbf{R}_i, \mathbf{C}_i, i = 1, \dots, q$ are matrices that operate on the rows and columns of $\mathbf{\Gamma}$, respectively. The non-separable gradient penalty in (16) is thus obtained when $\mathbf{P}_1, \mathbf{P}_2$, and \mathbf{P}_3 correspond to the finite differences of $\gamma(\mathbf{x}, t)$ along x, y and t respectively; \mathbf{R}_i and \mathbf{C}_i are the corresponding finite difference matrices.

Gao et al., have recently used a linear combination of sparse and a low-rank matrices [26] to model the dynamic imaging dataset and recover it from undersampled measurements. They chose the regularization parameters such that the low-rank component is essentially the static background signal. The dynamic components are assumed to be sparse in a pre-selected basis/frame, which is enforced by a convex sparsity prior. The use of a sparse model to capture the dynamic components is conceptually more similar to classical compressed sensing dynamic imaging schemes [27], [28], [29] (with the exception of the static component) than the proposed scheme. We have shown that the basis functions estimated from the data itself (using low-rank recovery) are more effective in representing the data compared to preselected basis functions, especially when respiratory motion is present [5]. We plan to compare the proposed scheme with the model in [26] and other state of the art dynamic imaging schemes in the future.

B. Algorithm formulation

We now derive a fast MM algorithm to solve (13). Specifically, we majorize the penalty terms by quadratic functions of $\mathbf{\Gamma}$:

$$\phi(\mathbf{\Gamma}) = \min_{\mathbf{W}} \frac{\beta_1}{2} \|\mathbf{\Gamma} - \mathbf{W}\|_F^2 + \eta(\mathbf{W}), \quad (18)$$

$$\begin{aligned} \psi(\mathbf{\Gamma}) = & \min_{\{\mathbf{Q}_i, i=1, \dots, q\}} \frac{\beta_2}{2} \sum_{i=1}^q \|\mathbf{R}_i \mathbf{\Gamma} \mathbf{C}_i - \mathbf{Q}_i\|_F^2 \\ & + \theta \left(\sqrt{\sum_{i=1}^q |\mathbf{Q}_i|^2} \right) \end{aligned} \quad (19)$$

Here, \mathbf{W} and $\mathbf{Q}_i, i = 1, \dots, q$, are auxiliary matrix variables and $\|\mathbf{\Gamma}\|_F$ is the Frobenius norm of $\mathbf{\Gamma}$. By definition, $\eta(\mathbf{W})$ and $\theta(\sqrt{\sum_i |\mathbf{Q}_i|^2})$ are matrix functions that are dependent on $\phi(\mathbf{W})$ and $\varphi(\mathbf{P})$ respectively.

Analytical expressions for η and θ can be derived in many cases as shown below. However, we find in Section IV that analytical expressions for η and θ are not required for efficient implementation. Using the above majorizations, we simplify the original cost function in (13) as

$$(\mathbf{\Gamma}, \mathbf{W}, \{\mathbf{Q}_i\})_{\text{opt}} = \arg \min_{\mathbf{\Gamma}, \mathbf{W}, \{\mathbf{Q}_i\}} \mathcal{C}(\mathbf{\Gamma}, \mathbf{W}, \mathbf{Q}_i) \quad (20)$$

where

$$\begin{aligned} \mathcal{C} = & \|\mathcal{A}(\mathbf{\Gamma}) - \mathbf{y}\|^2 \\ & + \frac{\lambda_1 \beta_1}{2} \|\mathbf{\Gamma} - \mathbf{W}\|_F^2 + \frac{\lambda_2 \beta_2}{2} \sum_{i=1}^q \|\mathbf{R}_i \mathbf{\Gamma} \mathbf{C}_i - \mathbf{Q}_i\|_F^2 \\ & + \lambda_1 \eta(\mathbf{W}) + \lambda_2 \theta \left(\sqrt{\sum_{i=1}^q |\mathbf{Q}_i|^2} \right) \end{aligned} \quad (21)$$

We propose to use an iterative alternating minimization scheme to minimize the above criterion. Specifically, we alternatively minimize (21) with respect to each of the variables, assuming others to be fixed. We denote the n^{th} iterate of these variables as $\mathbf{\Gamma}_n$, \mathbf{W}_n , and $\mathbf{Q}_{i,n}; i = 1, \dots, q$, respectively. One iteration of this scheme is described below.

- 1) Derive $\mathbf{\Gamma}_{n+1}$, assuming $\mathbf{W} = \mathbf{W}_n, \mathbf{Q}_i = \mathbf{Q}_{i,n}$:

$$\begin{aligned} \mathbf{\Gamma}_{n+1} = & \arg \min_{\mathbf{\Gamma}} \|\mathcal{A}(\mathbf{\Gamma}) - \mathbf{y}\|^2 + \frac{\lambda_1 \beta_1}{2} \|\mathbf{\Gamma} - \mathbf{W}_n\|_F^2 \\ & + \frac{\lambda_2 \beta_2}{2} \sum_{i=1}^q \|\mathbf{R}_i \mathbf{\Gamma} \mathbf{C}_i - \mathbf{Q}_{i,n}\|_F^2 \end{aligned} \quad (22)$$

Since this expression is quadratic in $\mathbf{\Gamma}$, we derive the analytical solutions for many measurement operators in Section IV.

- 2) Derive \mathbf{W}_{n+1} , assuming $\mathbf{\Gamma} = \mathbf{\Gamma}_{n+1}$:

$$\mathbf{W}_{n+1} = \arg \min_{\mathbf{W}} \frac{\beta_1}{2} \|\mathbf{\Gamma}_{n+1} - \mathbf{W}\|_F^2 + \eta(\mathbf{W}) \quad (23)$$

The optimal \mathbf{W} is thus obtained as the proximal mapping of $\mathbf{\Gamma}_{n+1}$, corresponding to the spectral penalty η . We derive analytical expressions for this step for the widely used nuclear norm and Schatten-p functionals in Section IV.

- 3) Derive $\mathbf{Q}_{i,n+1}$, assuming $\mathbf{\Gamma} = \mathbf{\Gamma}_{n+1}$:

$$\begin{aligned} \mathbf{Q}_{i,n+1} = & \arg \min_{\mathbf{Q}_i} \frac{\beta_2}{2} \sum_{i=1}^q \|\mathbf{R}_i \mathbf{\Gamma}_{n+1} \mathbf{C}_i - \mathbf{Q}_i\|_F^2 \\ & + \theta \left(\sqrt{\sum_{i=1}^q |\mathbf{Q}_i|^2} \right) \end{aligned} \quad (24)$$

The optimal $\{\mathbf{Q}, i = 1, \dots, q\}$ is thus the proximal mapping of $\{\mathbf{R}_i \mathbf{\Gamma}_{n+1} \mathbf{C}_i; i = 1, \dots, q\}$, associated with the matrix penalty θ . Since θ is non-separable, the corresponding shrinkage involves the simultaneous processing of the component matrices $\mathbf{R}_i \mathbf{\Gamma}_{n+1} \mathbf{C}_i; i = 1, \dots, q$. This step also has analytical expressions, as shown in section IV.

C. Expression of $\eta(\mathbf{W})$

We now focus on determining the function η , such that the majorization of the spectral penalty term in (18) holds. Since analytical expressions for η and θ are not essential to realize an efficient algorithm, readers may skip this section and go directly to Section IV.

We reorder the terms in (18) to obtain

$$\underbrace{\frac{\|\mathbf{\Gamma}\|_F^2}{2} - \frac{\phi(\mathbf{\Gamma})}{\beta_1}}_{g(\mathbf{\Gamma})} = \max_{\mathbf{W}} \left[\langle \mathbf{\Gamma}, \mathbf{W} \rangle - \underbrace{(\|\mathbf{W}\|_F^2/2 + \eta(\mathbf{W})/\beta_1)}_{f(\mathbf{W})} \right] \quad (25)$$

Here, $\langle \mathbf{W}, \mathbf{\Gamma} \rangle = \text{trace}(\mathbf{W}^T \mathbf{\Gamma})$ is the innerproduct of two matrices. From the theory in [22], the above relation is satisfied if $g(\mathbf{\Gamma})$ is a convex function and $f = g^*$ is the convex dual of g :

$$g^*(\mathbf{W}) = \max_{\mathbf{\Gamma}} (\langle \mathbf{W}, \mathbf{\Gamma} \rangle - g(\mathbf{\Gamma})). \quad (26)$$

Note that ϕ need not be convex for the above relation to hold. This majorization is valid if $g(\mathbf{\Gamma})$ is convex, which is possible even when ϕ is concave. Thanks to the property of unitarily invariant functions, the dual of a specified matrix function $g(\mathbf{\Gamma}) = \sum \mu_g(\sigma_i(\mathbf{\Gamma}))$ is obtained as

$$f(\mathbf{W}) = \sum \mu_g^*(\sigma_i(\mathbf{W})). \quad (27)$$

Thus, $\mu_f(\cdot) = \mu_g^*(\cdot)$ is the convex conjugate of $\mu_g(\cdot)$. From the above relations, we have $\eta(\mathbf{W}) = \sum \mu_\eta(\sigma_i(\mathbf{W}))$, where $\mu_\eta(x) = \beta_1 (\mu_f(x) - x^2/2)$.

We now approximate the non-differentiable ϕ penalties by continuously differentiable Huber functionals. These approximations are required to ensure that $g(\mathbf{\Gamma})$ is convex. In addition, differentiability of ϕ also provides additional simplifications.

- 1) Nuclear norm: We approximate the nuclear norm penalty $\|\mathbf{\Gamma}\|_* = \sum_i \sigma_i(\mathbf{\Gamma})$ as $\phi_{\beta_1}(\mathbf{\Gamma}) = \sum_i \mu_{\phi_{\beta_1}}(\sigma_i(\mathbf{\Gamma}))$.

Here, $\mu_{\phi_{\beta_1}}(x)$ is the standard scalar Huber function

$$\mu_{\phi_{\beta_1}}(x) = \begin{cases} |x| - 1/2\beta_1 & \text{if } x \geq \frac{1}{\beta_1} \\ \beta_1 |x|^2 / 2 & \text{else} \end{cases} \quad (28)$$

Note that $\phi_{\beta_1}(\mathbf{\Gamma}) \rightarrow \|\mathbf{\Gamma}\|_*$ as $\beta_1 \rightarrow \infty$. With this choice, the corresponding $g(\mathbf{\Gamma}) = \sum \mu_g(\sigma_i(\mathbf{\Gamma}))$ is given by

$$\mu_g(x) = \begin{cases} \frac{1}{2} \left(x - \frac{1}{\beta_1}\right)^2 & \text{if } x \geq \frac{1}{\beta_1} \\ 0 & \text{else} \end{cases} \quad (29)$$

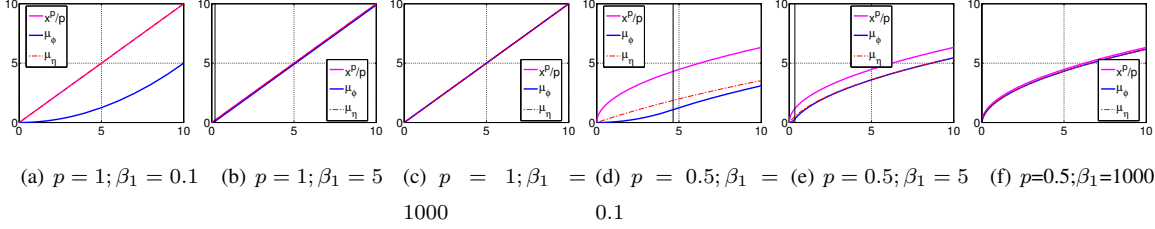


Fig. 1. Huber approximation of the spectral penalty and the corresponding η function. Note that the approximation of the original spectral penalty by the Huber function improves with increasing values of β . Clearly, large values of β are required to approximate Schatten p -norms; $p < 1$. It is observed that $\eta(x) = |x|, \forall \beta$ when $p = 1$. Hence, the variable splitting interpretation (see Section IV-E) is equivalent to the MM scheme. However, this equivalence breaks down when $p < 1$. Specifically, $\eta(\mathbf{\Gamma}) \rightarrow \|\mathbf{\Gamma}\|_p^p$ only when $\beta \rightarrow \infty$.

Note that g is convex for any β_1 . Using the property of convex conjugate functions described earlier, we find in the Appendix that $\mu_\eta = w$. Thus, we have $\eta(\mathbf{W}) = \|\mathbf{W}\|_*$, $\forall \beta_1$.

2) Schatten p norm: We approximate the Schatten p matrix norm by the corresponding Huber matrix function:

$$\mu_{\phi_{\beta_1}}(x) = \begin{cases} \frac{x^p}{p} - 1/(2\alpha\beta_1^\alpha) & \text{if } x \geq \beta_1^{1/(p-2)} \\ \beta_1 x^2/2 & \text{else} \end{cases} \quad (30)$$

Here, $\alpha = p/(2-p)$. The threshold specified by $\beta_1^{1/(p-2)}$ and the constant $1/(2\alpha\beta_1^\alpha)$ is chosen such that $\mu_{\phi_{\beta_1}}$ is continuously differentiable and μ_g is convex. The above formula is essentially an extension of the generalization proposed by [24] to matrix functionals. It is difficult to derive analytical expressions for $\mu_\eta(w)$ for arbitrary $p < 1$. However, we can numerically solve for $x = \partial_x \mu_g$ and evaluate $\mu_\eta(w)$ for specific values of w , as shown in Fig. 1. We show in the next section that analytical expressions for the proximal mapping, specified by (23), can be derived even if analytical expressions for η are not available.

We plot μ_ϕ , μ_η and x^p/p for $p = 1$ and $p = 0.5$ for different values of β_1 in Fig. 1. Note that $\mu_\eta(x) = |x|, \forall \beta_1$, when $p = 1$. However, $\mu_\eta(x)$ is different from $|x|^p/p$ when $p < 1$. This implies that the variable splitting interpretation of the majorize minimize algorithm breaks down when $p < 1$, as explained in Section IV.

D. Expression for θ

The Huber approximation of the total variation norm ($p_2 = 1$) was considered in [30], where they showed that

$$\theta \left(\sqrt{\sum_{i=1}^q |\mathbf{Q}_i|^2} \right) = \sqrt{\sum_{i=1}^q |\mathbf{Q}_i|^2}; \quad \forall \beta_2 \quad (31)$$

Analytical expressions of θ cannot be obtained when $p_2 < 1$. However, we derive the analytical expression for the shrinkage in Section IV, which will enable the efficient implementation.

IV. NUMERICAL ALGORITHM

We now focus on the numerical implementation of the three main subproblems. Specifically, we show that all of the three steps can be either solved analytically or using efficient algorithms for most penalties and measurement operators of practical interest. This enables us to realize a computationally efficient algorithm. We also introduce a continuation scheme to accelerate the convergence of the algorithm.

A. *Quadratic subproblem, specified by (22)*

Since the subproblem (22) is entirely quadratic, we rewrite it as a Tikhnonov regularized image recovery problem:

$$\begin{aligned} \gamma_{n+1} = \arg \min_{\gamma} & \|\mathcal{A}(\gamma) - \mathbf{y}\|^2 + \frac{\lambda_1 \beta_1}{2} \|\gamma - \mathbf{w}_n\|^2 \\ & + \frac{\lambda_2 \beta_2}{2} \sum_{i=1}^q \|\mathcal{G}_i(\gamma) - \mathbf{q}_{n,i}\|^2 \end{aligned} \quad (32)$$

Here, $\gamma \leftrightarrow \mathbf{\Gamma}$ and $\mathbf{q}_i \leftrightarrow \mathbf{Q}_i$ are the 3-D datasets, corresponding to the corresponding Casoratti matrices. Similarly, \mathcal{G}_i is the linear operator such that $\mathcal{G}_i(\gamma) \leftrightarrow \mathbf{R}_i^* \mathbf{\Gamma} \mathbf{C}_i$. We obtain the Euler-Lagrange equation of this variational problem as

$$\begin{aligned} & \left(\mathcal{A}^* \mathcal{A} + \lambda_1 \beta_1 \mathcal{I} + \lambda_2 \beta_2 \sum_{i=1}^q \mathcal{G}_i^* \mathcal{G}_i \right) \gamma_{n+1} \\ & = \mathcal{A}^* \mathbf{y} + \lambda_1 \beta_1 \mathbf{w}_n + \lambda_2 \beta_2 \sum_{i=1}^q \mathcal{G}_i^* \mathbf{q}_{n,i}. \end{aligned} \quad (33)$$

Here \mathcal{I} is the identity operator. Note that the variables in the right hand side of (33) are fixed. Thus, this step involves the solution to a linear system of equations. In the general setting, this system of equations can be solved efficiently using iterative algorithms such as conjugate gradient (CG). A few CG steps are often sufficient for good convergence since the algorithm is initialized by the previous iterate γ_n . We now show that analytical solutions of (32) do exist for many measurement operators. When the TV penalty is used, the above equation can be rewritten as

$$(\mathcal{A}^* \mathcal{A} + \lambda_1 \beta_1 \mathcal{I} + \lambda_2 \beta_2 \Delta) \gamma_{n+1} = \mathcal{A}^* \mathbf{y} + \lambda_1 \beta_1 \mathbf{w}_n + \lambda_2 \beta_2 p_n. \quad (34)$$

Here, $\Delta \gamma_{n+1}$ is the 3-D Laplacian of γ_{n+1} and $p_n = \nabla \cdot \mathbf{q}_n$ is the divergence of the vector field \mathbf{q}_n .

- **Fourier sampling:** An analytical expression can be derived for (32), when the measurements are Fourier samples of γ on a Cartesian grid. Specifically, we assume that the index set corresponding to the measured samples to be indicated by Λ and the corresponding measurements to be b_i ; i.e., $(b_i = \hat{\gamma}(\boldsymbol{\omega}_i))$, where $\hat{\gamma}$ is the discrete Fourier transform of γ). We split the frequency samples, specified by $\boldsymbol{\omega}$, into two sets Λ and Λ^c and evaluate the discrete Fourier transform of both sides of (34) to obtain:

$$\hat{\gamma}_{n+1}(\boldsymbol{\omega}_i) = \begin{cases} \frac{b_i + \lambda_1 \beta_1 \hat{w}_n(\boldsymbol{\omega}_i) + \lambda_2 \beta_2 \hat{p}_n(\boldsymbol{\omega}_i)}{1 + \lambda_1 \beta_1 + \lambda_2 \beta_2 \|\boldsymbol{\omega}_i\|^2} & \text{if } \boldsymbol{\omega}_i \in \Lambda \\ \frac{\lambda_1 \beta_1 \hat{w}_n(\boldsymbol{\omega}_i) + \lambda_2 \beta_2 \hat{p}_n(\boldsymbol{\omega}_i)}{\lambda_1 \beta_1 + \lambda_2 \beta_2 \|\boldsymbol{\omega}_i\|^2} & \text{else .} \end{cases} \quad (35)$$

Here, $p_n = \nabla \cdot \mathbf{q}_n$.

- **Deconvolution:** Convolution can be posed as a multiplication in the Fourier domain. Considering the Fourier transform of the matrix, (34) can be solved in the Fourier domain as

$$\hat{\gamma}_{n+1}(\boldsymbol{\omega}) = \frac{\hat{H}(\boldsymbol{\omega})^* \hat{b}(\boldsymbol{\omega}) + \lambda_1 \beta_1 \hat{w}_n(\boldsymbol{\omega}) + \lambda_2 \beta_2 \hat{p}_n(\boldsymbol{\omega})}{|\hat{H}(\boldsymbol{\omega})|^2 + \lambda_1 \beta_1 + \lambda_2 \beta_2 \|\boldsymbol{\omega}\|^2}. \quad (36)$$

Here, $H(\boldsymbol{\omega})$ is the transfer function of the blurring filter, $\boldsymbol{\omega}$ is the frequency, $\hat{b}(\boldsymbol{\omega})$ is the Fourier transform of the measured blurred image dataset and $\hat{p}_n(\boldsymbol{\omega})$ is the Fourier transform of $\nabla \cdot \mathbf{q}_n$.

B. Subproblem 2, specified by (23)

We will now focus on (23) and derive the analytical expression for \mathbf{W}_{n+1} :

$$\begin{aligned} \mathbf{W}_{n+1} &= \arg \min_{\mathbf{W}} \overbrace{\beta \|\mathbf{\Gamma}_{n+1}\|^2/2 + \beta \|\mathbf{W}\|_F^2/2 - \beta \langle \mathbf{\Gamma}_{n+1}, \mathbf{W} \rangle}^{\frac{\beta}{2} \|\mathbf{\Gamma}_n - \mathbf{W}\|_F^2} \\ &\quad + \eta(\mathbf{W}) \\ &= \arg \max_{\mathbf{W}} \beta \langle \mathbf{\Gamma}_{n+1}, \mathbf{W} \rangle - \underbrace{\beta (\|\mathbf{W}\|_F^2/2 + \eta(\mathbf{W})/\beta)}_{f(\mathbf{W})} \end{aligned} \quad (37)$$

The minimizer of this expression satisfies

$$\mathbf{\Gamma}_{n+1} = \beta \nabla f(\mathbf{W}_{n+1}). \quad (38)$$

We used the differentiability of ϕ , and hence f to obtain the above expression. This is valid for the Huber approximations of the spectral penalties. Since f and g are convex conjugates, ∇f and ∇g are inverse functions [19], [31]. Thus, we obtain the optimal \mathbf{W} that solves (37) as

$$\begin{aligned} \mathbf{W}_{n+1} = \nabla f^{-1}(\mathbf{\Gamma}_{n+1}) &= \nabla g(\mathbf{\Gamma}_{n+1}) \\ &= \mathbf{\Gamma}_{n+1} - \partial\phi(\mathbf{\Gamma}_{n+1})/\beta. \end{aligned} \quad (39)$$

We used the relation $g(\mathbf{\Gamma}) = \|\mathbf{\Gamma}\|_F^2/2 - \phi(\mathbf{\Gamma})/\beta$ in the second step. Thus, analytical expressions for η are not required to derive the shrinkage step, thanks to the property of convex conjugate functions. We now derive the shrinkage steps for specific spectral penalties.

- Special case: nuclear norm

$$\partial\mu_\phi(x) = \begin{cases} \text{sign}(x) & \text{if } |x| \geq \frac{1}{\beta_1} \\ \beta_1 x & \text{else.} \end{cases} \quad (40)$$

We assume $\mathbf{\Gamma} = \sum_{i=1}^{\min(m,n)} \sigma_i \mathbf{u}_i \mathbf{v}_i^H$ to be the singular value decomposition of $\mathbf{\Gamma}$. Substituting in (39), we get

$$\mathbf{W}^* = \sum_{i=1}^{\min(m,n)} (\sigma_i - 1/\beta_1)_+ \mathbf{u}_i \mathbf{v}_i^H, \quad (41)$$

where, $\mathbf{u}_i, \mathbf{v}_i, \sigma_i$ are the singular vectors and singular values of $\mathbf{\Gamma}$.

- Schatten p-norms Following the same steps, we obtain the shrinkage step for Schatten p-norms as ,

$$\mathbf{W}^* = \partial g(\mathbf{\Gamma}) = \sum_{i=1}^{\min(m,n)} \left(\sigma_i - \sigma_i^{(p_1-1)}/\beta_1 \right)_+ \mathbf{u}_i \mathbf{v}_i^H. \quad (42)$$

C. Solving the subproblem 3, specified by (24)

Problems similar to (24) has been addressed in the context of iterative algorithms for total variation minimization [30] and its non-convex variants [24]. The generalized shrinkage rule to derive $\mathbf{Q}_i; i = 1, \dots, q$ is specified by

$$\mathbf{Q}_{i,n+1} = \frac{(\mathbf{P} - \mathbf{P}^{(p_2-1)}/\beta_2)}{\mathbf{P}} \mathbf{R}_i \mathbf{\Gamma} \mathbf{C}_i, \quad (43)$$

where $\mathbf{P} = \sqrt{\sum_{i=1}^q |\mathbf{R}_i \mathbf{\Gamma}_{n+1} \mathbf{C}_i|^2}$. \mathbf{P}^p is the matrix whose elements are the p^{th} power of the entries of \mathbf{P} .

D. Continuation to improve the convergence

The three-step alternating minimization algorithm involves a tradeoff between convergence and accuracy. Specifically, when $\beta_1 = \beta_2 = 0$, (21) simplifies to three decoupled problems in Γ , \mathbf{W} and $\{\mathbf{Q}_i, i = 1, \dots, q\}$. Since all of these problems have analytical solutions, the entire algorithm converges in a single step to the minimum norm solution, which is a poor approximation of (13); this is expected since the corresponding Huber function is a poor approximation to the original cost function. In contrast, the approximation is exact when $\beta_1 = \beta_2 = \infty$. However, it is easy to see that the algorithm fails to converge in this case.

The above mentioned tradeoff between convergence and accuracy can be understood in terms of (i) the ability of the Huber function to approximate the original penalty and (ii) the proximity of the majorizing function to the Huber approximation. We illustrate this issue in Fig. 2 in the context of the nuclear norm penalty. Note that for small values of β , the Huber approximation $\mu_\phi(\sigma)$ of $|\sigma|$ is poor. However, the corresponding quadratic majorizing function $\beta(x-w)^2 + \mu_\eta(\sigma)$ closely approximates μ_ϕ . Hence, the MM scheme converges fast to the minimum of the approximate penalty. In contrast, when $\beta \rightarrow \infty$, the Huber function approximates the spectral penalty well, resulting in good accuracy of the final solution. However, the convergence is poor in this case since the approximation of the Huber function by the majorizing quadratic function is poor.

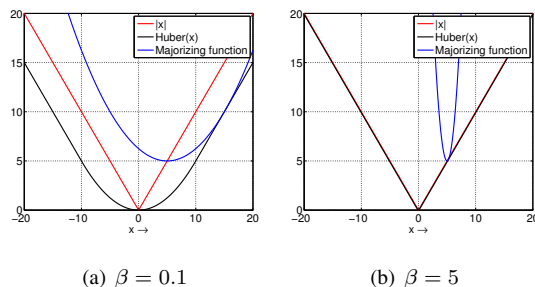


Fig. 2. Effect of β_1 on convergence and accuracy: We demonstrate the approximation of $|x|$ by the corresponding Huber penalty. Note that for $\beta = 0.1$, the majorizing function approximates the Huber function well, resulting in fast convergence to the minimum of the corresponding penalty. However, in this case the approximation of $|x|$ by the Huber function is poor resulting in poor accuracy. In contrast, the approximation of $|x|$ by the Huber function is good when $\beta = 5$. In this case, the majorizing function of the Huber function is a poor approximation. Specifically, it is too narrow, resulting in slow convergence.

To overcome the above mentioned tradeoff, we introduce a continuation scheme. Specifically, we initialize β_1 and β_2 with small values and progressively increase them, until convergence. The algorithm converges very fast for small values of β_1 and β_2 , as discussed before. We use the solution at each step to initialize the next step. For each choice of continuation parameters, we iterate the algorithm to convergence (i.e., until the relative change in the cost function in (13) is less than a pre-specified threshold). In all the experiments considered in this paper, we initialize the continuation parameters as $\beta_1 = \beta_2 = 5$ and increase them by a factor of five for each iteration of the outer loop.

E. Interpretation as a variable splitting scheme

The majorize-minimize scheme to solve for the spectrally regularized matrix recovery may be interpreted as a variable splitting (VS) strategy [6], similar to such schemes in compressed sensing [32], [33]:

$$\begin{aligned} \mathbf{\Gamma}^* &= \arg \min_{\mathbf{\Gamma}, \mathbf{W}} \|\mathcal{A}(\mathbf{\Gamma}) - \mathbf{b}\|^2 + \lambda_1 \phi(\mathbf{W}) \\ &\text{s.t. } \mathbf{\Gamma} = \mathbf{W} \end{aligned} \quad (44)$$

Here, \mathbf{W} is an auxiliary variable and the above constrained optimization problem is equivalent to (13), when $\lambda_2 = 0$. VS algorithms convert the above constrained optimization problem to an unconstrained problem by introducing an additional quadratic penalty:

$$(\mathbf{\Gamma}, \mathbf{W})^* = \arg \min_{\mathbf{\Gamma}, \mathbf{W}} \|\mathcal{A}(\mathbf{\Gamma}) - \mathbf{b}\|^2 + \lambda_1 \phi(\mathbf{W}) + \lambda_1 \frac{\beta_1}{2} \|\mathbf{\Gamma} - \mathbf{W}\|_F^2 \quad (45)$$

This unconstrained problem is equivalent to (44), when $\beta_1 \rightarrow \infty$. Note that (45) is very similar to (21) with $\lambda_2 = 0$, except that the ϕ is used instead of η . The VS scheme and the MM scheme are exactly the same when $p = 1$, since $\eta(\mathbf{W}) = \|\mathbf{W}\|_*$, $\forall \beta_1$. However, $\eta(\mathbf{W}) \neq \|\mathbf{W}\|_p^p$ when $p < 1$ (see Fig. 1). Hence, the two schemes are not equivalent for general Schatten p-norms.

The standard practice in VS compressed sensing schemes is to alternatively minimize the criterion with respect to each of the unknowns, assuming the other variable to be fixed [32], [33]. Thus, we obtain \mathbf{W}_{n+1} as

$$\mathbf{W}_{n+1} = \arg \min_{\mathbf{W}} \frac{\beta_1}{2} \|\mathbf{\Gamma}_{n+1} - \mathbf{W}\|_F^2 + \phi(\mathbf{W}) \quad (46)$$

When $\phi(\mathbf{\Gamma}) = \|\mathbf{\Gamma}\|_*$ [1], this proximal mapping can be efficiently implemented using singular value soft-thresholding. However, analytical closed form expressions for the above proximal mapping do not exist when non-convex spectral penalties (e.g. Schatten p norms; $\phi(\mathbf{\Gamma}) = \|\mathbf{\Gamma}\|_p^p$) are used. [Iterative algorithms may be used to solve this proximal mapping. However, it will be computationally more expensive since it involves an additional inner loop. Ehler recently demonstrated that approximating the the proximal mapping of non-convex \$\ell_p\$ penalties with hard thresholding shrinkage rules will provide computationally efficient solutions \[20\].](#) Adapting these approximate rules to non-convex spectral penalties, we get

$$\mathbf{W}_{n+1} = \sum_{i=1}^{\min(m,n)} \chi(\sigma_i) \mathbf{u}_i \mathbf{v}_i^H, \quad (47)$$

The thresholding function in (47) is defined as

$$\chi(\sigma_i) = \begin{cases} \sigma_i - \frac{2p c_p}{\beta_1} & \text{if } \sigma_i > \frac{2c_p}{\beta_1} \\ 0 & \text{else .} \end{cases} \quad (48)$$

where $c_p = 2^{p-2} \left(\frac{(2-p)^{2-p}}{(1-p)^{1-p}} \right)$ and $\mathbf{u}_i, \mathbf{v}_i$ and σ_i are the singular vectors and values of $\mathbf{\Gamma}_{n+1}$, respectively. A similar approximate rule can be used for the non-convex TV penalty. In contrast to these approximate rules, analytical shrinkage formulas can be derived for most spectral penalties $\eta(\mathbf{\Gamma})$ in the MM framework (see (39)). We compare the MM algorithm and the VS scheme with the approximate shrinkage rule in the results section; we observe that the proposed MM scheme provides faster convergence.

The MM scheme in the non-convex ($p_1 < 1; p_2 < 1$) case may be alternatively interpreted as an approximate VS algorithm, where (42) and (43) are used to approximate the corresponding proximal mappings; this approximation is not reported before and are only inspired by the MM formulation. The approximation is exact only when $\beta_1 = \beta_2 = \infty$ (see Fig. 1). The above approximate variable splitting scheme (with approximate MM-inspired proximal mappings) can be further accelerated using augmented-Lagrangian (AL) or split-Bregman (SB) methods [34], [35] as we have shown in [36]. Unlike conventional AL or SB methods (originally developed for convex penalties), the proposed non-convex schemes still require continuation since the approximation is only exact as $\beta_1, \beta_2 \rightarrow \infty$ (see Fig. 1.)

V. RESULTS

We will demonstrate the utility of the combined non-convex penalty in reliably recovering a sparse and low-rank matrix in Section V-A. The convergence of the algorithm and the utility of continuation will be studied in Section V-B. In Section V-C, we demonstrate the utility of the combined non-convex penalty in recovering dynamic contrast enhanced MR images from their undersampled Fourier measurements. The dynamic MRI dataset is only approximately low-rank and sparse.

A. Recovery of a low-rank and sparse matrix

We first demonstrate the benefits in using the combination of two non-convex penalties, compared to widely used nuclear norm scheme. We consider the recovery of the MIT logo from its sparse measurements to illustrate the algorithm. This image matrix (size of 46×81 with 3726 pixels) is ideal for our study since it is low-rank (rank = 5) and also has sparse gradients. Note that the signal is naturally a matrix and hence we do not use Casoratti matrix formulation as in (11). We use random measurement matrices and vary the number of measurements M from 100

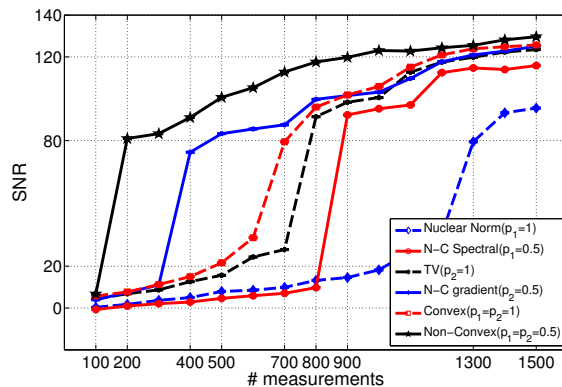


Fig. 3. Utility of the combination of non-convex penalties. We plot the SNR as a function of the number of measurements on the MIT logo, recovered using the six algorithms. Note that the SNR increases abruptly when the number of measurements exceeds a specified threshold. It is seen that the algorithms using the non-convex spectral (red solid curve) and non-convex TV penalty (blue solid curve) alone reduce the number of measurements required to recover the image considerably over their convex counterparts (blue dotted and black dotted curves, respectively). We also observe that the combination of the convex (red dotted) and non-convex (black solid) penalties work much better than the individual penalties.

M	$p_1=0.5$	$p_2=1$	$p_1=p_2=1$	$p_1=p_2=0.5$
200				
700				
800				
900				

Fig. 4. Sample recovered images for four different number of measurements using: Non-convex spectral penalty ($p_1 = 0.5$), standard TV ($p_2 = 1$), combination of convex penalties ($p_1 = p_2 = 1$), combination of non-convex penalties ($p_1 = p_2 = 0.5$). The rows correspond to different number of measurements. The results show that almost perfect reconstruction can be obtained when the number of measurements is larger than 200 by using the combination of both non-convex penalties ($p_1 = p_2 = 0.5$). Note that this is 6 times lower than using only the nuclear norm penalty (1300 measurements) and 4 times lower than standard TV (800 measurements). Similarly, we obtain a four fold improvement over non-convex spectral penalty alone.

to 1500 as in [1]. The matrix was then recovered from these measurements using (13) with six different parameter settings:

- 1) nuclear norm penalty alone ($p_1 = 1; \lambda_2 = 0$).
- 2) non-convex spectral penalty alone ($p_1 = 0.5; \lambda_2 = 0$).
- 3) standard TV penalty alone ($\lambda_1 = 0; p_2 = 1$).
- 4) non-convex gradient penalty alone ($\lambda_1 = 0; p_2 = 0.5$).
- 5) combination of both convex penalties ($p_1 = p_2 = 1$).
- 6) combination of both non-convex penalties ($p_1 = p_2 = 0.5$).

We repeat each experiment for ten different random measurement ensembles and evaluate the average signal to noise ratio (SNR), specified as

$$\text{SNR} = 20 \log \left(\frac{\|\mathbf{\Gamma}_{\text{orig}}\|_F}{\|\mathbf{\Gamma}_{\text{rec}} - \mathbf{\Gamma}_{\text{orig}}\|_F} \right). \quad (49)$$

For each setting, we optimize the regularization parameters (λ_1 and λ_2) with respect to SNR. Fig. 3 shows the SNR of the recovered image as a function of the number of measurements. It is seen that the SNR rises abruptly when the number of measurements exceeds a specified threshold. An SNR of 80 dB corresponds to almost perfect reconstruction.

We observe that the algorithm with the conventional nuclear norm scheme can perfectly recover the image, if the number of measurements is greater than 1300; these findings are consistent with the results in [1]. In contrast, the non-convex spectral penalty alone requires only 900 measurements. Similarly, the algorithm with the non-convex TV penalty alone requires only 400 measurements to perfectly recover the image, compared to 800 with standard TV.

These results demonstrate the benefit in using non-convex penalties over convex schemes. We did not encounter any local minima issues. We believe that the continuation strategy, where the cost function is initialized as a quadratic criterion and gradually made non-convex, minimizes the local minima problems.

It is seen that the combined convex penalty (TV and nuclear norm) requires approximately 700 measurements, compared to 1300 with nuclear norm alone and 800 with TV alone. Similarly, the combination of the non-convex penalties requires only 200 measurements, compared to 900 with non-convex spectral penalty alone and 400 with non-convex gradient penalty alone. These experiments demonstrate a significant reduction in the number of measurements required to recover a matrix, when sparsity and spectral penalties are combined. As described earlier, sparsity and low-rank properties are complementary; since the degrees of freedom of matrices that are simultaneously sparse and low-rank are small, the joint penalty is capable of significantly reducing the number of measurements. Sample images of recovered matrices for four different number of measurements are shown in Fig. 4.

B. Convergence of the algorithm

We now study the effect of the parameters β_1 and β_2 on the convergence of the algorithm and the accuracy of the solution. We consider the recovery of the MIT logo from $M = 1000$ measurements using the combined non-convex penalties ($p_1 = p_2 = 0.5$). We plot the evolution of the original cost function in (13) and SNR with respect to the number of iterations in Fig. 5.(a) and (b), respectively. It is observed that lower values of β_1 and β_2 result in fast convergence, but yield solutions with higher cost and lower SNR. This is expected since (21) is a poor approximation to (13). In contrast, higher values of β_1 and β_2 approximate the original cost function well, but result in slow convergence. We observe that the proposed continuation scheme, where β_1 and β_2 are initialized with small values and are gradually increased, offers the best compromise. In this specific example, the continuation scheme converged in 599 iterations. In contrast, the schemes with fixed values of β_1 and β_2 require far more number of iterations. The images recovered after 500 iterations using different parameter choices are shown in Fig. 6. We study the effect of different continuation schemes with different convergence rates in Fig. 7. We use fixed incrementing strategies in the first three experiments, where β_1 and β_2 are incremented by a fixed β_{inc} . We also tried several dynamic scheduling schemes. The fourth experiment shows the one with comparative best results, where β_{inc} is increased at each outer iteration; see caption of Fig. 7 for details. The plots show that the different schemes converge to the same solution, but the convergence rates are dependent on the specific continuation strategy. Note that the convergence rate of the algorithms do not vary significantly with the specific continuation strategy, indicating that the algorithm is not very sensitive to the specific update rule.

We compare the proposed MM algorithm with the approximate VS scheme in the context of spectrally regularized non-convex criterion in Fig. 8. Here, we set $\lambda_2 = 0$. The VS scheme relies on the approximate shrinkage rule, specified by (47). We compare the algorithms for $p_1 = 0.3$ and $p_1 = 0.5$, respectively. We consider $M = 1500$ measurements in (a), while $M = 1000$ measurements are studied in (b). It is observed that the MM scheme (blue and black solid curves) significantly outperforms the approximate VS scheme (red and magenta dotted curves),

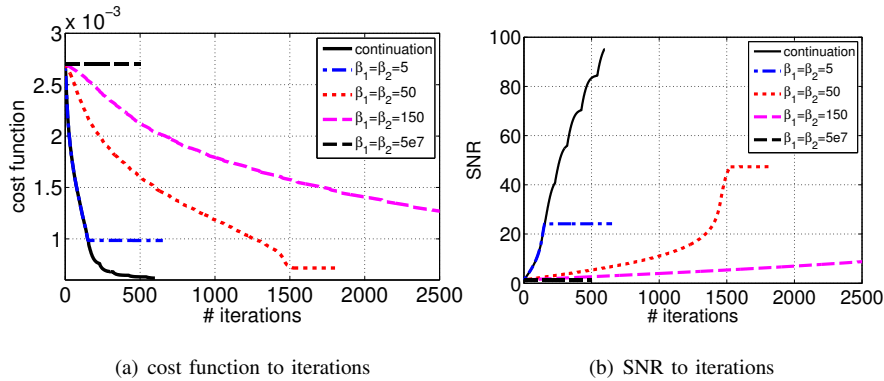


Fig. 5. Utility of the continuation scheme: We plot the cost and SNR as a function of the number of iterations. We observe that lower values of the parameters ($\beta_1 = \beta_2 = 5$) result in a very fast convergence, but yield a solution with higher cost and lower SNR. Higher values of the parameters improve the accuracy at the expense of the number of iterations. Note that the continuation strategy, where the parameters are initialized with $\beta_1 = \beta_2 = 5$ and increased by a factor of 5 within the outer loop, results in fast convergence and solutions with good SNR. We terminate the algorithm when the cost does not change, where the convergence is achieved with $\beta_1 = \beta_2 = 5e7$. We observe that the algorithm fails to converge if it is initialized with these parameters.

especially when p_1 and M are small. This experiments clearly demonstrate the utility of the MM scheme for non-convex penalties. As discussed earlier, both the algorithms are essentially the same when $p = 1$.

C. Accelerating dynamic contrast enhanced MRI

In this section, we illustrate the utility of the proposed algorithm in accelerating dynamic contrast enhanced (DCE) MRI. DCE MRI tracks the dynamic variations in the image intensity, resulting from the passage of a tracer bolus. Specifically, the paramagnetic tracer within the vasculature results in spin dephasing, hence resulting in decreased signal intensity. DCE MRI has shown great potential in diagnosing malignant lesions in the brain, breast and other organs. High temporal resolution is required to accurately estimate the kinetic parameters, while high spatial resolution is required to visualize the lesion morphology. Several acceleration schemes have been proposed to accelerate DCE MRI [37], [38]. The accelerations offered by these schemes are modest (2-3 fold), leaving room for further improvement.

We demonstrate the utility of the proposed non-convex scheme in significantly accelerating DCE MRI. The

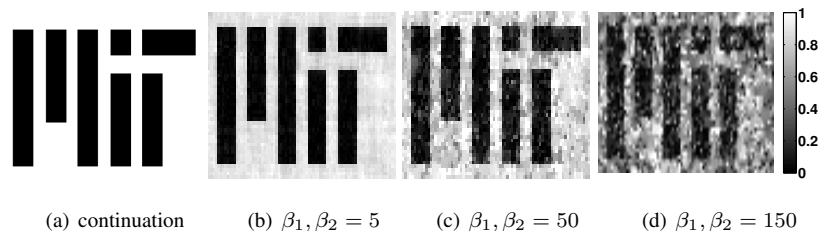


Fig. 6. Utility of continuation schemes in matrix recovery. We reconstruct the MIT logo with continuation and different fixed values of β . We show the reconstructions using (a) continuation scheme (initialized with $\beta_1 = \beta_2 = 5$ and gradually increased by a factor of 5) SNR=100.64; (b) $\beta_1 = \beta_2 = 5$, SNR=22.41; (c) $\beta_1 = \beta_2 = 50$, SNR=12.14; (d) $\beta_1 = \beta_2 = 150$, SNR=5.98 after 500 iterations. Note that the continuation scheme provides almost perfect recovery, while the other methods result in artifacts.

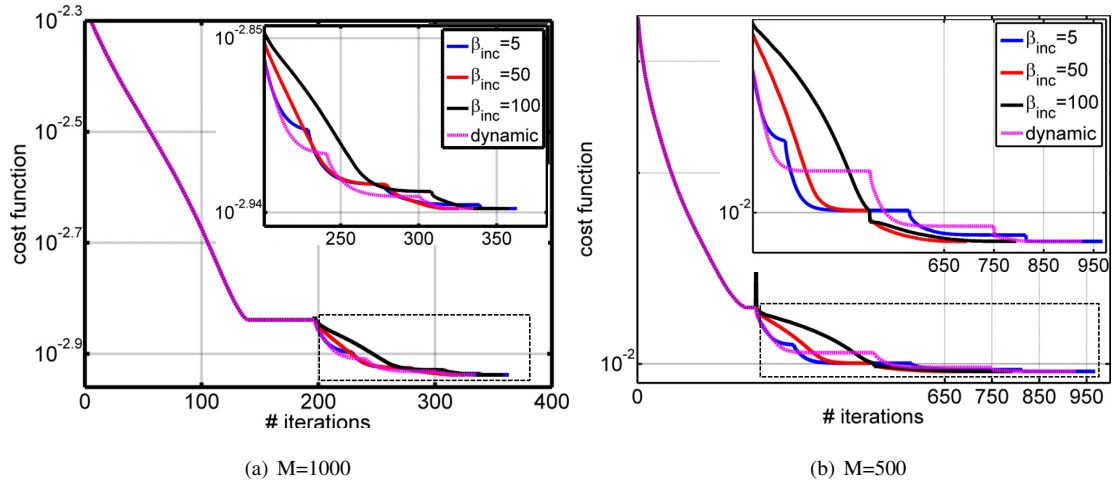


Fig. 7. Comparison of continuation strategies. We consider four continuation schemes that start with the same initial value of β_1 and β_2 . The first three are static schemes, where $\beta_1(n+1) = \beta_1(n) \cdot \beta_{inc}$ and $\beta_2(n+1) = \beta_2(n) \cdot \beta_{inc}$. We set β_{inc} to be 5, 50 and 100 in these three experiments. In the fourth scheme (dynamic continuation), we increase β_{inc} in a linear fashion. Specifically, we update β_{inc} as $\beta_{inc}(n) = 10 * n$; we studied several dynamic strategies and this choice resulted in the fastest convergence. The decrease in cost function are shown in the plots. The first iteration is the same for all algorithms since all the algorithms start with the same initialization. The zoomed portions of the curves are shown in the insets. We observe that the final result the algorithms converge to are the same. In addition, the convergence rate of the different continuation strategies does not vary significantly; this indicates that the algorithm does not require significant tuning of the continuation strategy.

dynamic MRI measurements correspond to the samples of the signal in Fourier $(k-t)$ space, corrupted by noise:

$$\mathbf{b}_i = \int_{\mathbf{x}} \gamma(\mathbf{x}, t_i) \exp(-j\mathbf{k}_i^T \mathbf{x}) d\mathbf{x} + \mathbf{n}_i; \quad i = 1, \dots, s.$$

Here, (\mathbf{k}_i, t_i) indicates the i^{th} sampling location. We denote the set of sampling locations as $\Xi = \{(\mathbf{k}_i, t_i), i = 1, \dots, s\}$. The fully sampled 3-D dataset of a single slice is shown in Fig. 10.(a); the data corresponds to sixty time

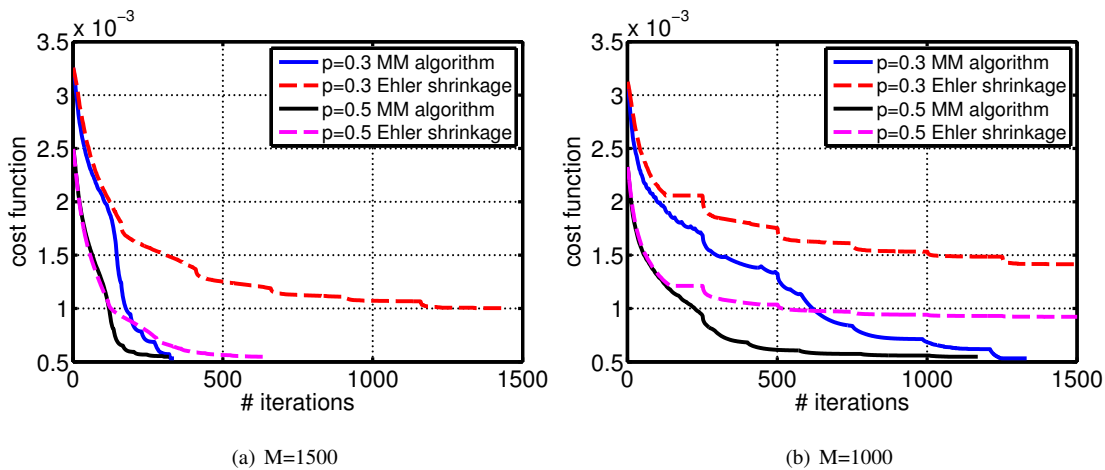


Fig. 8. Comparison of approximate VS algorithm and MM algorithm for the recovery of the MIT logo from different number of measurements, indicated by M . Note that the convergence rate of the MM scheme (black and blue solid curves) is considerably faster than the approximate VS method (magenta and red dotted curves) that relies on the Ehler approximation, especially for low values of p . The differences between the two methods are larger when the number of measurements are smaller.

points, separated by $TR=2$ sec; the matrix size is $128 \times 128 \times 60$. We retrospectively resample each slice of the data in the Fourier domain using a uniform radial trajectory. The trajectory is rotated by a random angle for each frame to obtain an incoherent pattern (see Fig. 10.(b)). The number of lines per slice is chosen depending on the specified acceleration. For example, 20 k-space lines approximately corresponds to the acceleration factor of $A = 7$. We recover the dynamic imaging dataset from its undersampled Fourier measurements using the proposed scheme. We use a few steps of conjugate gradients algorithm to solve for (22) at each iteration, since the samples are not on the 3-D Cartesian grid. We use the previous iterate as an initial guess, thus the CG algorithm converges to the solution of (22) in a few steps. The recovery of the DCE MRI dataset using the MATLAB implementation of the proposed algorithm takes approximately eight minutes on an Intel quad core processor with an NVIDIA Tesla graphical processing unit (GPU). The computationally expensive components of the algorithm are implemented using Jacket [39].

The proposed algorithm has two regularization parameters λ_1 and λ_2 that control the quality of the reconstructions. The specific choice of the continuation parameters only influences the speed of convergence and will not determine the quality of the final solution as seen from Fig. 7. Since the fully sampled dataset is available in this experiment, we choose the regularization parameters that minimize the reconstruction error. Extensive literature is available on efficient schemes to choose the regularization parameters, when the ground truth is not available [40], [41]; we plan to adapt these methods to determine the optimal regularization parameters in the future. Our recent experience with myo-cardial perfusion MRI shows that the parameters optimized for a specific dataset will give good reconstructions for other datasets acquired with the same protocol.

The SNR of the recovered 3-D dataset as a function of the acceleration is plotted in Fig. 9. We observe that the best SNR is obtained when both the non-convex penalties are used, which is around 1.5 dB better than nuclear norm alone and 6 dB superior than TV alone. It is also seen that the combined non-convex penalty (solid black curve) gives reconstructions that are approximately 1-2 dB better than its convex counterpart (dotted red curve), especially at higher accelerations. These experiments demonstrate the utility of the combination of non-convex penalties in challenging practical applications. We show the slice corresponding to the peak of the perfusion contrast, recovered using TV, nuclear norm and the combined non-convex penalties, in Fig. 10.(c)-(e). The corresponding error images are shown in Fig. 10.(f)-(h), respectively. Here, we consider $A = 7$, which corresponds to 20 k-space lines/frame. We plot the average intensity variations of the recovered images from 5 pixels in the tumor region (green dot) and 5 pixels of the healthy tissue (red dot) in Fig. 10.(i)-(k), respectively. Note that the curve from the tumor region has a larger dip and a larger width compared to that of the healthy tissue. This is due to the higher microvessel density and the increased tortuosity of the vessels in the tumor regions. We observe that the combination of non-convex penalties gives good fit to the measured data. The seven fold acceleration without significant degradation in image quality is quite remarkable, especially since we are only assuming a single channel acquisition; we expect to further improve the signal quality and/or acceleration using 12 or 32 channel head arrays that are now available.

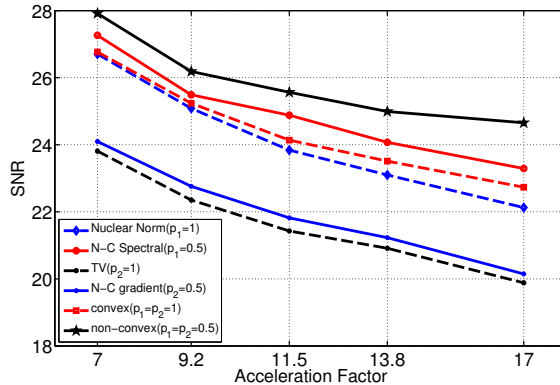


Fig. 9. SNR of the dynamic MRI dataset as a function to acceleration factor. We reconstruct the dataset from its Fourier samples using six methods: Nuclear Norm ($p_1 = 1$); non-convex spectral penalty ($p_1 = 0.5$); TV ($p_2 = 1$); non-convex gradient penalty ($p_2 = 0.5$), combined convex penalties ($p_1 = p_2 = 1$) and combined non-convex penalties ($p_1 = p_2 = 0.5$). Note that the combined non-convex penalty provides significant gains in SNR at almost all acceleration factors.

VI. CONCLUSION

We introduced a novel majorize-minimize algorithm to recover sparse and low-rank matrices from its noisy and undersampled measurements. We majorize the non-convex spectral and sparsity penalties in the cost function using quadratic matrix functions, resulting in an iterative three-step alternating minimization scheme. Since each of the steps in the algorithm has computationally efficient implementations, the algorithm provides fast convergence. We verified the utility of the combination of non-convex spectral and sparsity penalties to significantly reduce the number of measurements required for perfect recovery in dynamic MRI data, compared to current matrix recovery schemes.

VII. ACKNOWLEDGEMENTS

We thank the anonymous reviewers for their valuable comments that have significantly improved the quality of the manuscript.

VIII. APPENDIX 1

We derive the conjugate of the function μ_g , specified by (29) in this section. Specifically, μ_g^* is defined as

$$\begin{aligned} \mu_g^*(w) &= \max_x (wx - \mu_g(x)) \\ &= \max \left(\max_{x; x < \frac{1}{\beta}} wx, \max_{x; x > \frac{1}{\beta}} \left(wx - \frac{1}{2}(x - 1/\beta)^2 \right) \right) \end{aligned}$$

The maximum value of the first term ($wx; x < 1/\beta$) is given by w/β . The second term inside the bracket is true if $x = w + 1/\beta$, when the value of the function is given by $w^2/2 + w/\beta$. Since the second term is always greater than the first, we obtain

$$\mu_g^*(w) = \frac{w^2}{2} + \frac{w}{\beta} \quad (50)$$

Since $\mu_\eta(w) = \beta(\mu_g(w) - w^2/2)$, we have $\mu_\eta(w) = w$.

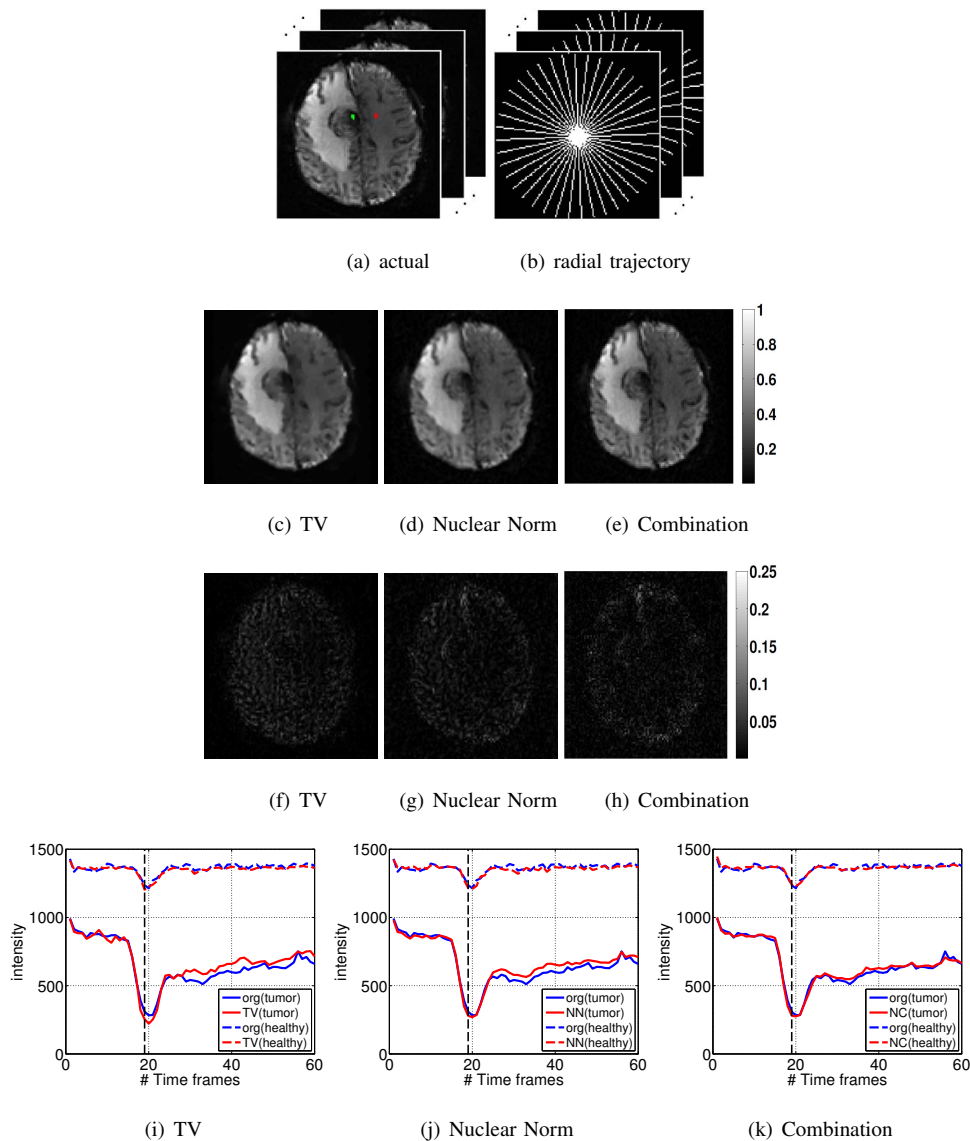


Fig. 10. Reconstruction of dynamic MRI data from undersampled Fourier samples. We consider 20 radial lines/image, which corresponds to an acceleration factor of $A = 7$. The images corresponding to the peak of the bolus (dotted line in the bottom row), which are recovered using TV ($p_2 = 1$), nuclear norm ($p_1 = 1$), and combination of non-convex penalties ($p_1 = p_2 = 0.5$) are shown in (c)-(e). The corresponding error images are shown in (f)-(h), respectively. (e), (h) and (k) correspond to the reconstructions using the proposed combination of non-convex penalties. The SNRs of the reconstructions using TV, Nuclear Norm, and combination of non-convex penalties are 23.81dB, 26.77dB, and 27.92dB, respectively. Note that the proposed scheme provides a 1-4 dB improvement in performance and considerably better image quality compared to the classical schemes.

REFERENCES

- [1] E. J. Candes and B. Recht, "Exact matrix completion via convex optimization," *Foundations of Computational Mathematics*, vol. 9, no. 6, pp. 717–772, 2009.
- [2] B. Recht, M. Fazel, and P. Parrilo, "Guaranteed minimum-rank solutions of linear matrix equations via nuclear norm minimization," *SIAM Rev.*, vol. 52, no. 3, pp. 471–501, 2010.
- [3] Z. Liang, "Spatiotemporal imaging with partially separable functions," in *Proceedings of the ISBI, 2007*, pp. 181–182.

- [4] C. Brinegar, Y. Wu, L. Foley, T. Hitchens, Q. Ye, C. Ho, and Z. Liang, "Real-time cardiac MRI without triggering, gating, or breath holding," in *IEEE EMBC*, 2008, pp. 3381–3384.
- [5] S. Goud, Y. Hu, E. Di Bella, and M. Jacob, "Accelerated dynamic mri exploiting sparsity and low-rank structure: kt slr," *IEEE Transactions on Medical Imaging*, vol. 30, no. 5, pp. 1042–1054, 2011.
- [6] S. Goud, Y. Hu, and M. Jacob, "Real-time cardiac MRI using low-rank and sparsity penalties," in *Proceedings of the ISBI*, 2010.
- [7] H. Pedersen, S. Kozerke, S. Ringgaard, K. Nehrke, and W. Y. Kim, "k-t pca: temporally constrained k-t blast reconstruction using principal component analysis," *Magn Reson Med*, vol. 62, no. 3, pp. 706–716, Sep 2009.
- [8] M. Lustig, D. Donoho, J. Santos, and J. Pauly, "Compressed sensing MRI," *Signal Processing Magazine, IEEE*, vol. 25, no. 2, pp. 72–82, 2008.
- [9] E. Candes, X. Li, Y. Ma, and J. Wright, "Robust principal component analysis," *preprint*, 2009.
- [10] B. Zhao, J. Haldar, and Z. Liang, "Psf model-based reconstruction with sparsity constraint: Algorithm and application to real-time cardiac mri," in *IEEE EMBC*. IEEE, 2010, pp. 3390–3393.
- [11] B. Zhao, J. Haldar, A. Christodoulou, and Z. Liang, "Further development of image reconstruction with joint partial separability and sparsity constraints," in *ISBI*. IEEE, 2011.
- [12] J. Trzasko and A. Manduca, "Relaxed conditions for sparse signal recovery with general concave priors," *IEEE Trans. SP*, vol. 57, no. 11, pp. 4347–4354, 2009.
- [13] R. Chartrand, "Exact reconstruction of sparse signals via nonconvex minimization," *IEEE Signal Processing Letters*, vol. 14, no. 10, pp. 707–710, 2007.
- [14] D. Wipf and S. Nagarajan, "Iterative reweighted l1 and l2 methods for finding sparse solutions," *IEEE J. select. Topics Signal Processing*, vol. 4, no. 2, pp. 317–329, 2010.
- [15] J. Cai, E. Candes, and Z. Shen, "A singular value thresholding algorithm for matrix completion," *SIAM J. Optim.*, vol. 20, pp. 1956–1982, 2010.
- [16] S. Ma, D. Goldfarb, and L. Chen, "Fixed point and bregman iterative methods for matrix rank minimization," *Mathematical Programming*, 05 2009.
- [17] K. Toh and S. Yun, "An accelerated proximal gradient method for nuclear norm regularized least squares," *Preprint*, 2009.
- [18] J. Huang, S. Zhang, and D. Metaxas, "Efficient mr image reconstruction for compressed mr imaging," *Medical Image Computing and Computer-Assisted Intervention–MICCAI 2010*, pp. 135–142, 2010.
- [19] R. T. Rockafellar and R.-B. Wets, *Variational Analysis*. Springer Verlag, 2004.
- [20] M. Ehler and S. Geisel, "Arbitrary shrinkage rules for approximation schemes with sparsity constraints," *Schloss Dagstuhl Seminar Proceedings - Structured Decompositions and Efficient Algorithms*, no. 08492, 2009.
- [21] J. Trzasko and A. Manduca, "Highly undersampled magnetic resonance image reconstruction via homotopic ell_0 -minimization," *IEEE Transactions on Medical Imaging*, vol. 28, no. 1, pp. 106–121, 2009.
- [22] A. S. Lewis, "The convex analysis of unitarily invariant matrix functions," *Journal of Convex Analysis*, vol. 2, no. 1, pp. 173–183, 1995.
- [23] J. Haldar and D. Hernando, "Rank-constrained solutions to linear matrix equations using powerfactorization," *IEEE Signal Processing Letters*, vol. 19, pp. 584–587, 2009.
- [24] R. Chartrand, "Fast algorithms for nonconvex compressive sensing: MRI reconstruction from very few data," in *Proceedings of the ISBI*, no. 262-265, 2009.
- [25] L. Rudin, S. Osher, and E. Fatemi, "Nonlinear total variation based noise removal algorithms," *Physica D: Nonlinear Phenomena*, vol. 60, no. 1-4, pp. 259–268, 1992.
- [26] H. Gao, J.-F. Cai, Z. Shen, and H. Zhao, "Robust principal component analysis based four-dimensional computed tomography," *Physics in Medicine and Biology*, vol. 56, pp. 3181–3198, 2011.
- [27] H. Jung, J. Park, J. Yoo, and J. C. Ye, "Radial k-t focuss for high-resolution cardiac cine MRI," *Magn Reson Med*, Oct 2009.
- [28] M. Lustig, J. Santos, D. Donoho, and J. Pauly, "kt SPARSE: High frame rate dynamic MRI exploiting spatio-temporal sparsity," in *Proceedings of the 13th Annual Meeting of ISMRM, Seattle*. Citeseer, 2006, p. 2420.
- [29] U. Gamper, P. Boesiger, and S. Kozerke, "Compressed sensing in dynamic mri," *Magnetic Resonance in Medicine*, vol. 59, no. 2, pp. 365–373, 2008.

- [30] Y. Wang, J. Yang, W. Yin, and Y. Zhang, "A new alternating minimization algorithm for total variation image reconstruction," *SIAM J. Imaging Sciences*, vol. 1, no. 3, pp. 248–272, 2008.
- [31] Legendre transformation. [Online]. Available: http://en.wikipedia.org/wiki/Legendre_transformation
- [32] M. Afonso, J. Bioucas-Dias, and M. Figueiredo, "An augmented lagrangian approach to the constrained optimization formulation of imaging inverse problems," *IEEE Trans. Image Processing*, vol. 19, no. 9, pp. 2345–2356, 2010.
- [33] —, "Fast image recovery using variable splitting and constrained optimization," *Arxiv preprint arXiv:0910.4887*, 2009.
- [34] E. Esser, "Applications of lagrangian-based alternating direction methods and connections to split bregman," *CAM report*, vol. 9, p. 31, 2009.
- [35] T. Goldstein and S. Osher, "The split bregman algorithm for l1 regularized problems," *UCLA CAM Report*, pp. 08–29, 2008.
- [36] S. Goud, Y. Hu, E. DiBella, and M. Jacob, "Accelerated first pass cardiac perfusion mri using improved k-t slr," in *ISBI*, 2011.
- [37] B. Madore, "Using UNFOLD to remove artifacts in parallel imaging and in partial-Fourier imaging," *Magn Reson Med*, vol. 48, no. 3, pp. 493–501, Sep 2002.
- [38] M. Han, B. L. Daniel, and B. A. Hargreaves, "Accelerated bilateral dynamic contrast-enhanced 3D spiral breast MRI using tsense," *J Magn Reson Imaging*, vol. 28, no. 6, pp. 1425–1434, Dec 2008.
- [39] Jacket: accelerating matlab using gpu. [Online]. Available: <http://www.accelereyes.com/products/jacket>
- [40] S. Ramani, T. Blu, and M. Unser, "Monte-carlo sure: A black-box optimization of regularization parameters," *IEEE Transactions on Image Processing*, vol. 17, no. 9, pp. 1540–1554, 2008.
- [41] O. Scherzer, "The use of morozov's discrepancy principle for tikhonov regularization for solving nonlinear ill-posed problems," *Computing*, vol. 51, no. 1, pp. 45–60, 1993.